



<b>Publication Year</b>	2018
<b>Acceptance in OA</b>	2020-11-13T12:54:37Z
<b>Title</b>	Galaxy-Galaxy Weak-lensing Measurements from SDSS. II. Host Halo Properties of Galaxy Groups
<b>Authors</b>	Luo, Wentao, Yang, Xiaohu, Lu, Tianhuan, Shi, Feng, Zhang, Jun, Mo, H. J., Shu, Chenggang, Fu, Liping, RADOVICH, MARIO, Zhang, Jiajun, Li, Nan, Sunayama, Tomomi, Wang, Lei
<b>Publisher's version (DOI)</b>	10.3847/1538-4357/aacaf1
<b>Handle</b>	<a href="http://hdl.handle.net/20.500.12386/28321">http://hdl.handle.net/20.500.12386/28321</a>
<b>Journal</b>	THE ASTROPHYSICAL JOURNAL
<b>Volume</b>	862



# Galaxy–Galaxy Weak-lensing Measurements from SDSS. II. Host Halo Properties of Galaxy Groups

Wentao Luo<sup>1</sup>, Xiaohu Yang<sup>1,2</sup>, Tianhuan Lu<sup>3</sup>, Feng Shi<sup>4</sup>, Jun Zhang<sup>1</sup>, H. J. Mo<sup>5,6</sup>, Chenggang Shu<sup>7</sup>, Liping Fu<sup>7</sup>,  
Mario Radovich<sup>8,9</sup>, Jiajun Zhang<sup>1</sup>, Nan Li<sup>10</sup>, Tomomi Sunayama<sup>11</sup>, and Lei Wang<sup>12</sup>

<sup>1</sup> Department of Astronomy, Shanghai Key Laboratory for Particle Physics and Cosmology, Shanghai Jiao Tong University, Shanghai 200240, People’s Republic of China; [wentao.luo82@sjtu.edu.cn](mailto:wentao.luo82@sjtu.edu.cn)

<sup>2</sup> IFSA Collaborative Innovation Center, and Tsung-Dao Lee Institute, Shanghai Jiao Tong University, Shanghai 200240, People’s Republic of China; [xyang@sjtu.edu.cn](mailto:xyang@sjtu.edu.cn)

<sup>3</sup> Zhiyuan College, Shanghai Jiao Tong University, Shanghai 200240, People’s Republic of China

<sup>4</sup> Shanghai Astronomical Observatory, Nandan Road 80, Shanghai 200030, People’s Republic of China

<sup>5</sup> Department of Astronomy, University of Massachusetts, Amherst, MA 01003-9305, USA

<sup>6</sup> Physics Department and Center for Astrophysics, Tsinghua University, Beijing 10084, People’s Republic of China

<sup>7</sup> Shanghai Key Lab for Astrophysics, Shanghai Normal University, 100 Guilin Road, 200234, Shanghai, People’s Republic of China

<sup>8</sup> INAF-Osservatorio Astronomico di Napoli, via Moiariello 16, I-80131 Napoli, Italy

<sup>9</sup> INAF-Osservatorio Astronomico di Padova, vicolo dell’Osservatorio 5, I-35122 Padova, Italy

<sup>10</sup> Centre for Astronomy & Particle Theory at the University of Nottingham, Nottingham NG7 2RD, UK

<sup>11</sup> Kavli Institute for the Physics and Mathematics of the Universe, The University of Tokyo 5-1-5 Kashiwanoha, Kashiwa, Chiba 277-8583, Japan

<sup>12</sup> Purple Mountain Observatory, Chinese Academy of Sciences, 8 Yuanhua Road, Nanjing, 210023, People’s Republic of China

Received 2017 December 25; revised 2018 May 22; accepted 2018 June 4; published 2018 July 17

## Abstract

In this second paper in a series studying galaxy–galaxy lensing signals using Sloan Digital Sky Survey Data Release 7 (SDSS DR7), we present our measurement and modeling of the lensing signals around groups of galaxies. We divide the groups into four halo mass bins and measure the signals around four different halo-center tracers: brightest central galaxies (BCGs), luminosity-weighted centers, number-weighted centers, and X-ray peak positions. For groups cross-identified in both X-ray and SDSS DR7, we further split the groups into low and high X-ray emission subsamples, both of which are assigned to two halo-center tracers, BCGs and X-ray peak positions. The galaxy–galaxy lensing signals show that BCGs, among the four candidates, are the best halo-center tracers. We model the lensing signals using a combination of four contributions: the off-center NFW host halo profile, subhalo contribution, stellar contribution, and projected two-halo term. We sample the posterior of five parameters, i.e., the halo mass, concentration, off-centering distance, subhalo mass, and fraction of subhalos, via a Monte Carlo Markov Chain (MCMC) package using the galaxy–galaxy lensing signals. After taking into account the sampling effects (e.g., Eddington bias), we found that the best-fit halo masses obtained from lensing signals are quite consistent with those obtained in the group catalog based on an abundance matching method, except in the lowest mass bin.

*Key words:* galaxies: clusters: general – gravitational lensing: weak

## 1. Introduction

Modern galaxy formation theory suggests that dark matter halos form first, providing gravitational potential for galaxies to form. The mass of dark matter halos is thus a critical quantity to understand galaxy formation and constrain the cosmological parameters. There are many methods that can be used to constrain halo mass in observations. The luminosity of the X-ray emission from the intracluster medium due to thermal bremsstrahlung is scaled with the dark matter halo mass assuming a hydroequilibrium state of the gas (Pratt et al. 2009). The Sunyaev–Zeldovich (Sunyaev & Zeldovich 1972) effect, i.e., the inverse Compton scattering between the high-energy electrons from clusters and the CMB photons, is another indicator of cluster mass (Bleem et al. 2015).

Clusters are optically selected from large photometric galaxy surveys with large sky coverages and large redshift ranges and assigned with dark matter halo masses. Based on SDSS, SDSS-C4 (Miller et al. 2005) and RedMaPPer (Rykoff et al. 2014) select clusters using photometric data alone, whereas the MaxBCG sample (Koester et al. 2007) adds spectroscopic redshift as extra information in the selection criteria. All of those samples use an empirical scaling relation between the effective number of member

galaxies (richness) and halo mass, a.k.a. the richness–mass relation, to assign halo masses to clusters. Such methods are mainly applicable to very massive clusters and need to be scaled with additional measurements.

Based on spectroscopic redshift surveys, galaxy groups can be extracted from halos of much lower mass either by the traditional friends-of-friends (FOF) method (e.g., Eke et al. 2004) or by a sophisticated adaptive halo-based group finder (e.g., Yang et al. 2005, 2007, hereafter Y07), which is more reliable in their membership determination. From the group catalogs, a wide variety of mass estimation methods have been developed. Y07 applied a luminosity ranking and stellar mass ranking method to estimate the halo mass. For poor systems, Lu et al. (2015) introduced an empirical mass estimation method applying the gap between the brightest central galaxy (BCG) luminosity and the satellite luminosity. By assuming a Gaussian velocity distribution, satellite kinematics (van den Bosch et al. 2004) measure the dynamical mass of galaxy groups. Similarly, galaxy infall kinematics (Zu & Weinberg 2013; Zu et al. 2014) can also be used to constrain the halo mass.

Weak gravitational lensing signal, though statistical in nature, is considered to be another powerful tool to study the

property of dark matter distributions, due to the fact that the signal is sensitive to all intervening mass between the observer and the source. The successful measurement of weak-lensing signals requires high-quality imaging of background galaxies. Many recent surveys like CFHTLenS (Heymans et al. 2012), DES (Jarvis et al. 2016), and KIDS (Kuijken et al. 2015; Viola et al. 2015), etc., have weak lensing as one of their key scientific projects. Future large surveys, either ground-based or space-based, such as *EUCLID* (Refregier et al. 2010) and LSST (LSST Science Collaboration et al. 2009), also have weak lensing as one of their key projects. The high-quality and deep galaxy survey images, in terms of galaxy number per square arcminute, enables measurements for second-order weak-lensing studies, a.k.a. the cosmic shear (Fu et al. 2008; Kilbinger et al. 2013), which are now constantly used to constrain cosmological parameters such as  $\sigma_8$  and  $\Omega_m$ .

The Sloan Digital Sky Survey (SDSS; York et al. 2000) initiated galaxy–galaxy lensing analysis following Fischer et al. (2000) and found that the final signal should be subtracted from the signal from the random sample. It was followed by Sheldon et al. (2004), who chose the SDSS main sample as lenses. Hirata & Seljak (2003) and Mandelbaum et al. (2005, 2006) not only studied the halo properties of lenses from the SDSS main sample, but also analyzed the sources of systematics caused by the point spread function (PSF), selection effect, and noise rectification effect. Simet et al. (2017) used redMaPPer as lenses and tested the consistency of the mass–richness relation. These galaxy–galaxy lensing signals provided us with another method to measure the halo masses of the lens systems under consideration.

To obtain reliable galaxy–galaxy lensing measurements, the accurate image processing of source galaxies is essential. Many groups have developed image processing pipelines devoted to improving the accuracy of shape measurements (Kaiser et al. 1995; Bertin & Arnouts 1996; Maoli et al. 2000; Rhodes et al. 2000; Bernstein & Jarvis 2002; Bacon & Taylor 2003; Hirata & Seljak 2003; Refregier 2003; Heymans et al. 2005; Zhang 2010, 2011; Bernstein & Armstrong 2014; Zhang et al. 2015). Among these are Lensfit (Miller et al. 2007, 2013; Kitching et al. 2008), which applies a Bayesian-based model-fitting approach; the Bayesian Fourier Domain method (Bernstein & Armstrong 2014), which carries out Bayesian analysis in the Fourier domain using the distribution of unlensed galaxy moments as a prior; and the Fourier\_Quad method developed by Zhang (2010, 2011, 2016) and Zhang et al. (2015), which uses image moments in the Fourier domain.

Very recently, Luo et al. (2017) have developed an image processing pipeline and applied it to SDSS DR7 imaging data. The galaxy–galaxy lensing signals were measured for lens galaxies that have been separated into different luminosity bins and stellar mass bins. As the second paper in this series, here we measure the galaxy–galaxy lensing signals using the group catalogs constructed by Yang et al. (2007). We will measure the galaxy–galaxy lensing signals around groups in different mass bins as well as for four types of halo-center tracers: BCGs, luminosity-weighted centers (LwCen), number-weighted centers (NwCen) and X-ray peak positions. We focus on the estimation of the halo properties of the groups under consideration, such as their halo masses, concentrations, and off-center effects, etc. The ultimate goals for this series of papers are twofold and will be pursued in our two subsequent probes. The first goal is to use

galaxy–galaxy lensing measurements to constrain cosmological parameters and conditional stellar mass functions of galaxies for eBOSS galaxies using the method outlined in van den Bosch et al. (2013), Shi et al. (2017), and Cacciato et al. (2013). The second goal is to constrain cosmological models by combining the dynamical mass and weak-lensing mass measurements around galaxy clusters in the C4 cluster catalog (Miller et al. 2005).

The structure of this paper is organized as follows. In Section 2, we first present the data set and the main results of galaxy–galaxy lensing signals measured around galaxy groups. We show our modeling and parameter constraints in Section 3. We discuss the Eddington bias that the group mass estimation may have in Section 4. We summarize our results in Section 5. Unless stated otherwise, we adopt an  $\Lambda$ CDM cosmology with  $\Omega_m = 0.28$ ,  $\Omega_\Lambda = 0.72$ , and  $h = 1.0$ .

## 2. The Galaxy–Galaxy Lensing Signals of Galaxy Groups

### 2.1. Sources

We use the shape catalog created by Luo et al. (2017) based on SDSS DR7 imaging data. The DR7 imaging data, with  $u$ ,  $g$ ,  $r$ ,  $i$ , and  $z$  bands, cover about 8423 square degrees of the LEGACY sky ( $\sim 230$  million distinct photometric objects). The total number of objects identified as galaxies is around 150 million. These galaxies are further selected and processed by our image pipeline. The galaxies are selected by OBJC\_TYPE=3 from PHOTO pipe (Lupton et al. 2001) and must be brighter than 22 in the  $r$ -band model magnitude and brighter than 21.6 in the  $i$ -band model magnitude. We also apply flags such as BINNED1 (detected at  $\geq 5$ ), SATURATED=0 (do not have saturated pixels), EDGE=0 (not located at the edge of the CCD), MAYBE\_CR=0 (not cosmic rays), MAYBE\_EGHOST=0 (not an electronic ghost line), and PEAKCENTER=0 (centroiding algorithm works well for this subject). In processing the images, the PSF effect was corrected by combining the Bernstein & Jarvis (2002) and Hirata & Seljak (2003) methods. After the shape measurement, a size cut by resolution factor ( $\mathcal{R} \geq 1/3$ ) was applied. The final shape catalog for our study contains 41,631,361 galaxies with position, shape, shape error, and photo- $z$  information.

### 2.2. Lenses

The galaxies used in our probe are obtained from the New York University Value-Added Galaxy Catalog (NYU-VAGC; Blanton et al. 2005), which is based on SDSS DR7 (Abazajian et al. 2009) but with an independent set of significantly improved reductions. From the NYU-VAGC, we select all galaxies in the main galaxy sample with an extinction-corrected apparent magnitude brighter than  $r = 17.72$ , with redshifts in the range  $0.01 \leq z \leq 0.20$ , and with redshift completeness  $C_z > 0.7$ . This gives a sample of 639,359 galaxies with a sky coverage of 7748 square degrees. For each galaxy, we estimate its stellar mass using the fitting formula of Bell et al. (2003).

From this galaxy catalog, a total of 472,113 groups are selected using the halo-based group finder (Yang et al. 2007), each of which has been assigned with a halo mass by the ranking method. With the halo mass information, we bin the groups with mass  $\geq 10^{12} M_\odot$  into four mass bins. Shown in the left panel of Figure 1 are the stellar mass distributions of all galaxies (green solid line) and BCGs in different halo mass bins as indicated. The related average values of these galaxies are

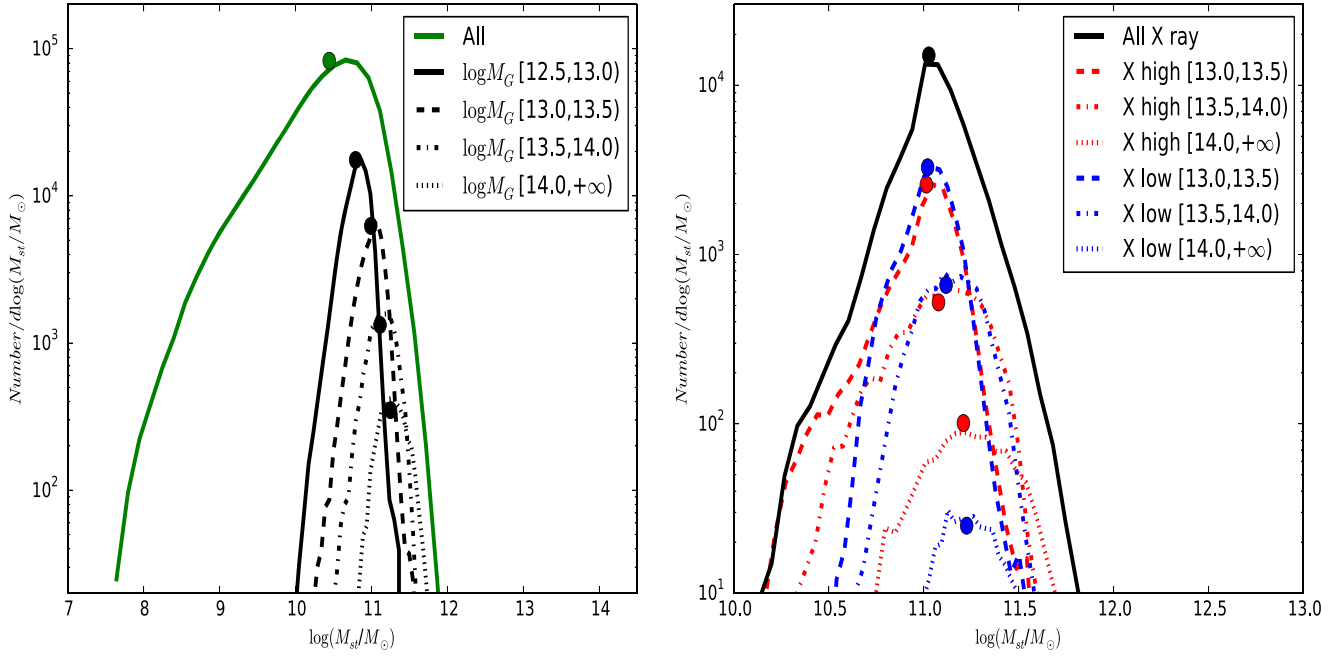


**Figure 1.** Left panel: the green solid line and the green dot denote the stellar mass distribution and the average stellar mass of all the galaxies, respectively. The black solid, dashed, dotted–dashed, and dotted lines and the black dots are the stellar mass distributions and average stellar masses of BCGs in the different halo mass bins, as indicated. Right panel: similar to the left panel, but here for high (red) and low (blue) X-ray luminosity subsamples.

shown as the solid dots on top of the lines. There is a monotonic increase of the average stellar mass of BCGs for the four mass bin groups. Table 1 lists some properties of the groups in these four mass bins. For each mass bin, we define four types of halo-center tracers i.e., BCG, LwCen, NwCen, and X-ray peak position (there is no X-ray measurement for the first mass bin).

For the three halo bins with halo mass  $\log M_G \geq 13.0$ , where  $M_G$  is the halo mass from the group catalog estimated using abundance matching, Wang et al. (2014) measured their X-ray luminosities using the *ROSAT* data. We divide groups in each of the mass bin into high X-ray luminosity and low X-ray luminosity subsamples with roughly equal numbers using the  $L_X$  parameter provided in the Wang et al. (2014) catalog, where  $L_X$  is the X-ray luminosity of a group in 0.2–2.4 keV in units of  $10^{44} \text{ erg s}^{-1}$ . Related information for these subsamples is listed in Table 2. There is a slight difference between the mean redshifts of the low X-ray luminosity and high X-ray luminosity subsamples. Both high and low X-ray luminosity samples are assigned BCGs and X-ray peak positions as their halo-center tracers. Note that Wang et al. (2014) only provided X-ray luminosity for groups with mass larger than  $10^{13.0} h^{-1} M_\odot$ , where the halo masses are estimated based on the ranking of characteristic group stellar mass. Here, however, we are using the group masses estimated using the ranking by characteristic group luminosity. Thus, some of our groups are not assigned X-ray luminosities due to the slight difference in the two mass estimations. For instance, in the low-mass bin, a group with a luminosity-ranked halo mass  $10^{13.0} h^{-1} M_\odot$  might have a halo mass of  $10^{12.9} h^{-1} M_\odot$  via stellar mass ranking. Then this group, which does not have X-ray measurements, is excluded from the lens sample. Thus, the total number of groups used in the high and low X-ray luminosity subsamples is slightly reduced, especially in the low-mass bin.

Shown in the right panel of Figure 1 are the stellar mass distributions of BCGs associated with the X-ray peak positions

**Table 1**  
Properties of the Four Lens Samples Created for This Paper

Sample	$\log M_G$	$N_{\text{grp}}$	$\langle z \rangle$	$\log \langle M_{\text{st}} \rangle$	$\log \langle M_G \rangle$
M1	(12.5, 13.0]	101042	0.13	10.77	12.72
M2	(13.0, 13.5]	43896	0.15	10.97	13.21
M3	(13.5, 14.0]	14707	0.15	11.10	13.70
M4	(14.0, $\infty$ ]	4033	0.15	11.25	14.25

**Note.** Columns 1–6 correspond to the sample name, group mass range, number of groups, average redshift, stellar mass, and group mass, respectively.

**Table 2**  
High/Low X-Ray Dichotomy

Mass Bin	$L_X$	$N_{\text{grp}}$	$\langle z \rangle$	$\log \langle M_{\text{st}} \rangle$	$\log \langle M_G \rangle$
13.0–13.5	high	14582	0.14	10.97	13.24
	low	22086	0.15	11.00	13.23
13.5–14.0	high	7285	0.14	11.05	13.71
	low	7049	0.16	11.12	13.68
14.0–above	high	2953	0.15	11.20	14.27
	low	1080	0.16	11.23	14.18

**Note.** Columns 1–6 correspond to the group mass range, X-ray luminosity status, number of groups, average redshift, stellar mass, and group mass, respectively.

in different halo mass bins as indicated. The dots on top of the lines are their average values. Here, results are shown for the low X-ray luminosity (blue) and high X-ray luminosity subsamples (red). Again, we see a monotonic increase of the average stellar mass of BCGs for the three mass bin groups.

### 2.3. Measuring the Galaxy–Galaxy Lensing Signals

The shear signals  $\gamma$  along any desired direction can be measured by the weighted mean of the source galaxy shapes (Mandelbaum et al. 2005; Luo et al. 2017),

$$\gamma_l = \frac{1}{2\bar{R}} \frac{\sum w_i e_l^{\text{rot}}}{\sum w_i}, \quad (1)$$

where  $l = 1, 2$ ;  $w_i$  is a weighting function; and  $e_l^{\text{rot}}$  is the ellipticity of background galaxies after SPA (the angle between the camera column position with respect to north from fpC files) rotation. Here,  $\bar{R}$  is the mean responsivity of our survey galaxies, which is calculated using Equations 5–33 to Equations 5–35 in Bernstein & Jarvis (2002). The weighting term is composed of two components,

$$w = \frac{1}{\sigma_{\text{sky}}^2 + \sigma_{\text{shape}}^2}, \quad (2)$$

where  $\sigma_{\text{shape}} = \langle e^2 \rangle$  is the shape noise and  $\sigma_{\text{sky}} = \frac{\sigma^{\text{pix}}}{\mathcal{R}F} \sqrt{4\pi n}$  is the sky noise. Here,  $\sigma^{\text{pix}}$  denotes the size of the galaxy in pixels,  $\mathcal{R}$  is the resolution factor,  $F$  is the flux, and  $n$  the sky and dark current in ADU.

The tangential shear of a lens system is connected to its excess surface density (ESD) through the geometric factor  $\Sigma_{\text{crit}}(z_l, z_s) = \frac{c^2}{4\pi G} \frac{D_s}{D_l D_s}$ ,

$$\Delta\Sigma(R) = \Sigma(\leq R) - \Sigma(R) = \gamma_t \Sigma_{\text{crit}}(z_l, z_s). \quad (3)$$

Here,  $z_l$  and  $z_s$  denote the redshifts of the group and the source, respectively.  $D_l$ ,  $D_s$ , and  $D_{ls}$  are the angular diameter distance of the lens and the source, and that between the lens and the source.  $\Sigma(\leq R)$  is the average surface density inside the projected distance  $R$ , and  $\Sigma(R)$  is the surface density at the projected distance  $R$ .

Shown in Figure 2 are the ESD profiles measured around groups in different halo mass bins as indicated in each panel. In each panel, results are shown for different halo-center tracers: BCG (black solid lines with the green band as the one sigma error), LwCen (black dotted line), NwCen (black dashed line), and X-ray peak position (black dashed–dotted line). Here, the error bars are obtained by 2000 bootstrap resamplings of the lens systems in consideration. The negative values from the measured ESDs are denoted in red. At smaller scales  $< 100 h^{-1}$  kpc, for more massive bins, the ESD signals around LwCen and NwCen begin to deviate from the signal around BCGs.

Shown in Figure 3 are the ESDs measured from the high and low X-ray luminosity groups. The solid curves with red one sigma error bands are the signals measured around the high X-ray luminosity subsamples while the dashed lines with blue one sigma bands are the results for the low X-ray luminosity subsamples. There are some differences between the ESDs of the high and low X-ray luminosity groups. In general, the high X-ray luminosity groups show overall higher amplitudes of ESDs, indicating that the masses of their host halos are somewhat more massive.

### 2.4. Boost Factor Correction

In our measurement, we also applied the boost factor correction (Johnston et al. 2007), which corrects for the contamination by stacking those source galaxies that are

actually associated with foreground clusters (Fischer et al. 2000). The definition of the boost factor is the weighted ratio between the number of galaxies around the lens sample and the random sample (Mandelbaum et al. 2005):

$$B(r) = \frac{n(r)}{n_{\text{rand}}(r)}. \quad (4)$$

The measured ESD signal is multiplied by  $B(r)$  to account for such an effect.

## 3. The Halo Properties of Galaxy Groups

With the ESDs measured for the different group samples and subsamples in the previous section, we proceed to constrain the related halo properties of galaxy groups in this section.

### 3.1. Weak-lensing Model

The ESD around a lens galaxy is related to the line-of-sight projection of the galaxy–matter cross-correlation function,

$$\xi_{\text{gm}}(r) = \langle \delta(\mathbf{x})_g \delta(\mathbf{x} + \mathbf{r})_m \rangle, \quad (5)$$

so that (e.g., Cacciato et al. 2009; More et al. 2013; van den Bosch et al. 2013)

$$\Sigma(R) = 2\bar{\rho} \int_R^\infty [1 + \xi_{\text{gm}}(r)] \frac{r dr}{\sqrt{r^2 - R^2}} \quad (6)$$

and

$$\Sigma(\leq R) = \frac{4\bar{\rho}}{R^2} \int_0^R y dy \int_y^\infty [1 + \xi_{\text{gm}}(r)] \frac{r dr}{\sqrt{r^2 - y^2}}, \quad (7)$$

where  $\bar{\rho}$  is the average background density of the universe. Note that in both equations, we have omitted the contribution from the mean density of the universe, as it does not contribute to the ESD. In general, the ESD is composed of the following four components: host halo mass, subhalo mass if it is a satellite or interloper, stellar mass associated with the galaxy under consideration, and projected two-halo term,

$$\Delta\Sigma(R) = \Delta\Sigma_{\text{host}}(R) + \Delta\Sigma_{\text{sub}} + \Delta\Sigma_{*}(R) + \Delta\Sigma_{2h}. \quad (8)$$

According to Yang et al. (2006), if the candidate lens galaxy (system) is located at the center of the host halo, the average projected density of the host halo can be calculated from the NFW profile (Navarro et al. 1997). Assuming an NFW profile of the host halo, we have

$$\rho(r) = \frac{\rho_0}{(r/r_s)(1 + r/r_s)^2}, \quad (9)$$

with  $\rho_0 = \frac{\bar{\rho} \Delta_{\text{vir}}}{3I}$ , where  $\Delta_{\text{vir}} = 200$  and  $I = \frac{1}{c^3} \int_0^c \frac{xdx}{(1+x)^2}$ . Here,  $c$  is the concentration parameter defined as the ratio between the virial radius of a halo and its characteristic scale radius  $r_s$ . The projected surface density can then be analytically expressed as (Yang et al. 2006)

$$\Sigma_{\text{NFW}}(R) = \frac{M_h}{2\pi r_s^2 I} f(x), \quad (10)$$

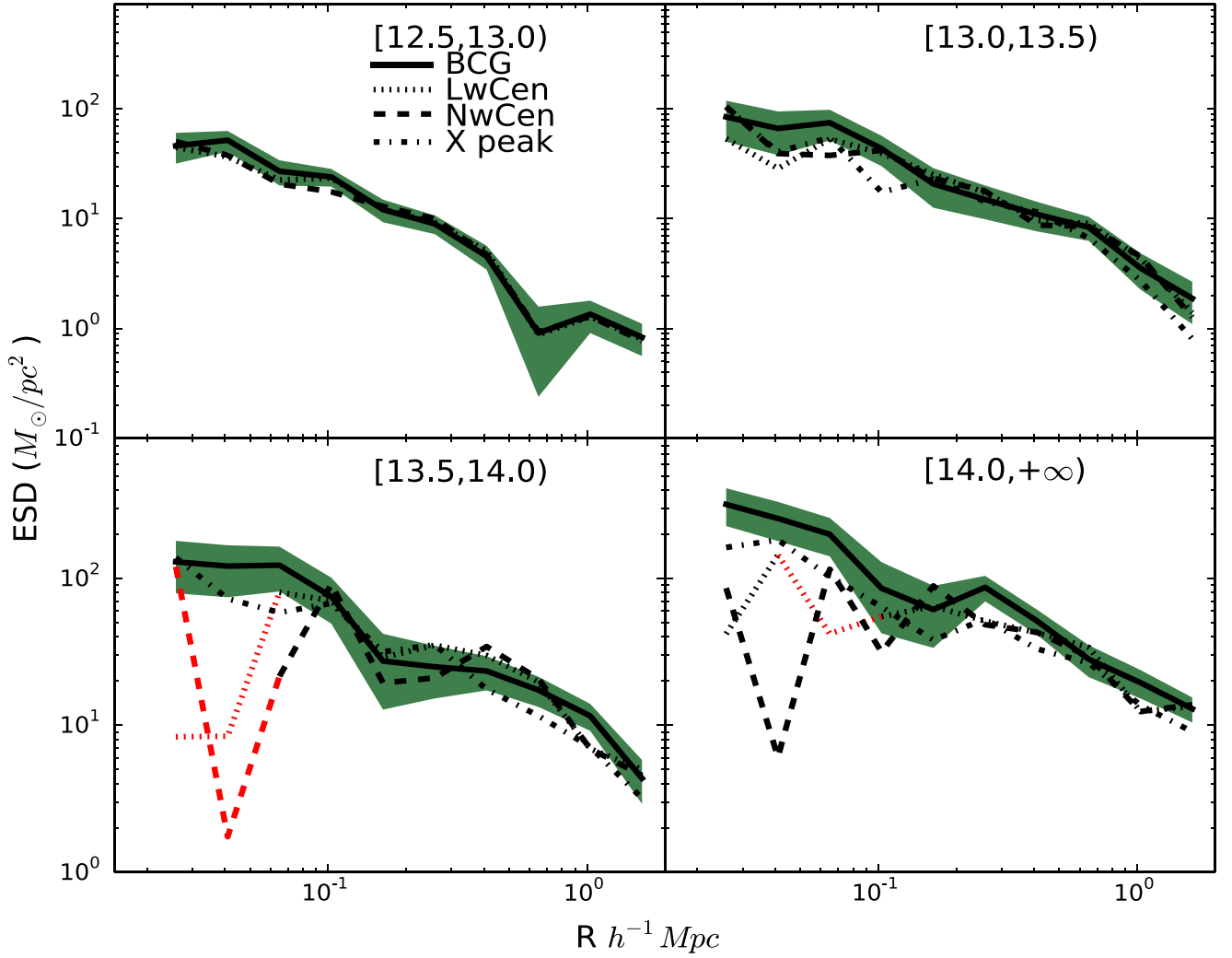


**Figure 2.** The ESD profiles measured from four mass bins along with different halo-center tracers. Solid lines with green shaded areas represent results for BCGs. The dotted, dashed, and dotted–dashed lines are the results for LwCens, NwCens, and X-ray peak positions, respectively. The red parts denote negative values.

where  $M_h$  is the halo mass, and  $f(x)$  has the following form with  $x = R/r_s$  (see Bartelmann 1996):

$$f(x) = \begin{cases} \frac{1}{x^2-2} \left[ 1 - \frac{\ln \frac{1+\sqrt{1-x^2}}{x}}{\sqrt{1-x^2}} \right] & x < 1 \\ \frac{1}{3} & x = 1 \\ \frac{1}{x^2-1} \left[ 1 - \frac{a \tan(\sqrt{x^2-1})}{\sqrt{x^2-1}} \right] & x > 1. \end{cases} \quad (11)$$

On the other hand, if the candidate lens galaxy is not located at the center of the host halo but at an off-center distance  $R_{\text{off}}$ , the projected surface density will change from an NFW profile  $\Sigma_{\text{NFW}}(R)$  to

$$\Sigma_{\text{host}}(R|R_{\text{off}}) = \frac{1}{2\pi} \int_0^{2\pi} \Sigma_{\text{NFW}}(\sqrt{R^2 + R_{\text{off}}^2 + 2R_{\text{off}}R \cos \theta}) d\theta. \quad (12)$$

Here, we adopt the offset model proposed by Johnston et al. (2007), where  $R_{\text{off}}$  follows a 2D Gaussian distribution. This model is drawn from the mock catalog based on the ADDGALS technique (Wechsler et al. 2006) combined with the light cone from the Hubble Volume simulation

(Evrard et al. 2002). The resulting projected density profile is the convolution between  $P(R_{\text{off}})$  and  $\Sigma_{\text{host}}(R|R_{\text{off}})$ ,

$$\Sigma_{\text{host}}(R|R_{\text{sig}}) = \int dR_{\text{off}} P(R_{\text{off}}) \Sigma_{\text{host}}(R|R_{\text{off}}), \quad (13)$$

where

$$P(R_{\text{off}}) = \frac{R_{\text{off}}}{R_{\text{sig}}^2} \exp(-0.5(R_{\text{off}}/R_{\text{sig}})^2). \quad (14)$$

Here,  $R_{\text{sig}}$  is the dispersion of  $P(R_{\text{off}})$ . Thus, in total, we have three free parameters of the host halo properties,  $M_h$ ,  $c$ , and  $R_{\text{sig}}$ , to be constrained using the observed ESDs. As an illustration, we show in the left panel of Figure 4 how the measured ESDs may vary as a function of  $R_{\text{sig}}$ . Here, we adopt a fixed halo mass and concentration with  $\log M_h = 14.0$  and  $c = 7.0$ , respectively, based on the Zhao et al. (2009) formula and vary  $R_{\text{sig}} = 0.05, 0.1, 0.2 h^{-1} \text{ Mpc}$ . A larger  $R_{\text{sig}}$  moves the ESD peak farther away from measurement center and suppresses the signal at small scale.

Next, we consider the subhalo contribution. Here we assume that a fraction  $f_{\text{sub}}$  of BCGs contains subhalos with mass

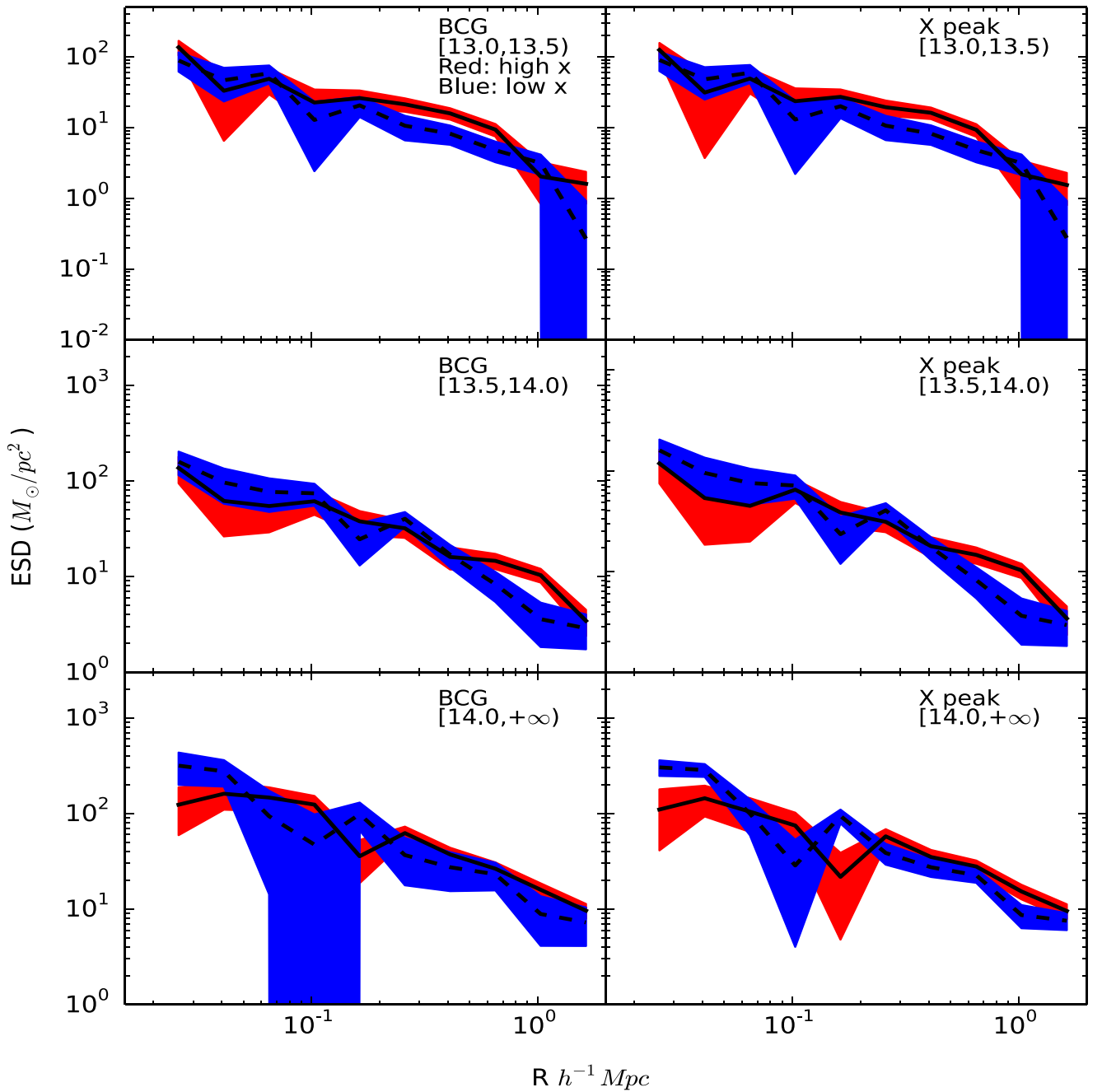


**Figure 3.** The ESD profiles measured from the high and low X-ray luminosity subsamples. From the top panel to the bottom panel, the mass increases as indicated in each panel. The black solid lines with red one sigma regions are the ESD profiles measured from X-ray luminous subsamples, while the dashed lines with blue one sigma regions denote the X-ray faint subsamples. The left and right columns are the results measured around BCGs and X-ray peak positions, respectively.

$\log M_{\text{sub}},$

$$\Sigma_{\text{sub}}(R) = f_{\text{sub}} \Sigma_{\text{NFW}}(R|M_{\text{sub}}, c = 15). \quad (15)$$

Here we simply fix the concentration as<sup>13</sup>  $c = 15$  and treat  $\log M_{\text{sub}}$  and  $f_{\text{sub}}$  as the fourth and fifth free parameters in our modeling. In addition, we require that  $\log M_h - \log M_{\text{sub}} \geq 0.3$  and  $f_{\text{sub}} \leq 1.0$ .

We then consider the stellar mass component. As pointed out in Johnston et al. (2007) and George et al. (2012), the stellar

mass component can be treated as a point mass, and the related ESD can be modeled simply as

$$\Delta \Sigma_*(R) = \frac{M_*}{2\pi R^2}, \quad (16)$$

where  $M_*$  is the stellar mass of the candidate BCGs under consideration. We directly use the average stellar mass of galaxies as given in Tables 1 and 2 in our modeling.

Finally, for the signal caused by the two-halo term, we calculate the power spectrum at the mean redshift of each sample using the Code for Anisotropies from Microwave Background of Lewis (2013) and then convert the power spectrum to the matter-matter correlation function  $\xi_{\text{mm}}$

<sup>13</sup> As subhalos are on average relatively low-mass ones and may be affected by the stripping effect, their concentration is thus set to relatively large values. Changing this value to 10 does not impact any of our results significantly.

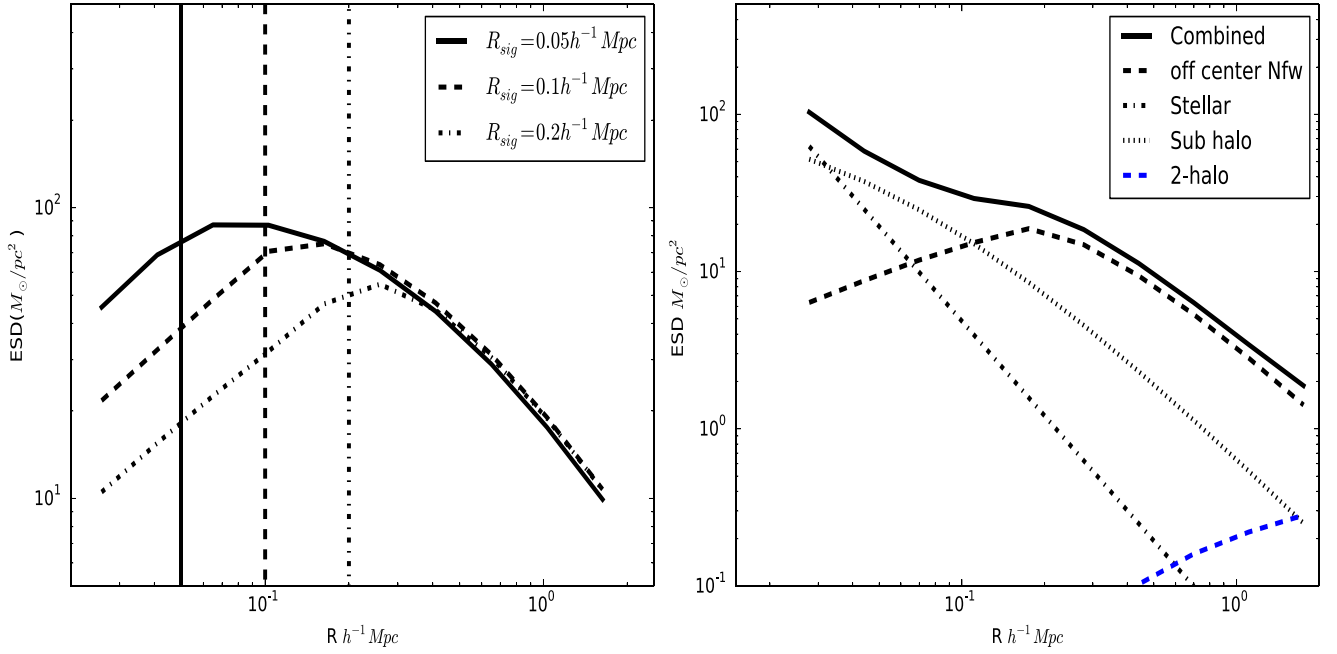


**Figure 4.** Left panel: the black line is the theoretical prediction of the ESD profile with  $R_{\text{sig}} = 0.05 h^{-1} \text{ Mpc}$ , while the dashed line and the dotted–dashed line are the ESD profiles with  $R_{\text{sig}} = 0.1$  and  $0.2 h^{-1} \text{ Mpc}$ , respectively. The three vertical lines denotes the  $R_{\text{sig}}$  values. Right panel: the model we adopt to describe the lensing ESD profile. The dashed, dotted, dotted–dashed, and blue dashed lines are the contributions from an off-centered NFW profile with  $R_{\text{sig}} = 0.1 h^{-1} \text{ Mpc}$ , the subhalo, the stellar mass of the galaxy under consideration, and the two-halo term, respectively. The black solid line is the combined profile.

(Takahashi et al. 2012).  $\xi_{\text{mm}}$  is then related to the halo–matter correlation function  $\xi_{\text{hm}}$  via the halo bias  $b_h(M_h)$  model (Seljak & Warren 2004),

$$\xi_{\text{hm}} = b_h(M_h)\xi_{\text{mm}} \quad (17)$$

To be more precise, we use the scale-dependent bias model of Tinker et al. (2005),

$$\xi_{\text{hm}} = b_h\eta\xi_{\text{mm}}, \quad (18)$$

where

$$\eta(r) = \frac{(1 + 1.17\xi_{\text{mm}}(r))^{1.49}}{(1 + 0.69\xi_{\text{mm}}(r))^{2.09}}. \quad (19)$$

The two-halo term projected mass density  $\Delta\Sigma_{2\text{halo}}(R)$  is then calculated using Equations (3), (6), and (7). In practice, we only make the integration to a distance  $50 h^{-1} \text{ Mpc}$  to model the two-halo term contribution (see also Niemiec et al. 2017).

As an illustration, we show in the right panel of Figure 4 each component of the model. Here we adopt  $\log M_h = 12.5$ ,  $c = 10.0$ ,  $\log M_{\text{sub}} = 11.0$ , and  $f_{\text{sub}} = 0.5$ . The off-centered NFW profile is shown as the dashed line, the stellar component as the dotted–dashed line, the subhalo as the dotted line, and the two-halo term as the blue dashed line. The combined signal is shown as the black solid curve. From this plot, we can see that at scales smaller than  $50 h^{-1} \text{ kpc}$ , the stellar contribution becomes significant. The two-halo term contribution is only important at scales larger than a few virial radii.

### 3.2. Constraining Halo Properties Using MCMC

In this subsection, we present how we constrained the halo properties using the above measured ESDs. There are five free parameters in our fitting process: host halo mass ( $\log M_h$ ), concentration ( $c$ ), off-center distance ( $R_{\text{sig}}$ ), subhalo mass ( $\log M_{\text{sub}}$ ), and subhalo fraction ( $f_{\text{sub}}$ ). We apply *emcee*

(<http://dan.iel.fm/emcee/current/>) to run a Monte Carlo Markov Chain (hereafter MCMC) to explore the likelihood function in the multidimensional parameter space.<sup>14</sup>

We assume a Gaussian likelihood function using a covariance matrix built from bootstrap sampling,

$$\ln \mathcal{L}(\mathbf{X}|\Theta) = -0.5((\mathbf{X} - D_{\text{model}})^T C^{-1}(\mathbf{X} - D_{\text{model}})) \quad (20)$$

where  $\mathbf{X}$  is the ESD data vector,  $D_{\text{model}}$  is the model, and  $C^{-1}$  is the inverse of the covariance matrix.  $\Theta$  denotes the parameters in the model.

In order to minimize the prior influence, we use broad flat priors for all five parameters. We set the halo mass range for each fitting mass bin to be  $[12.0, 16.0]$ , concentration range  $[1.0, 20.0]$ ,  $R_{\text{sig}}$  range  $[0.0-1.0]$ , and  $f_{\text{sub}}$  range  $[0.0-1.0]$ . The only physical assumption on the prior is that  $10.0 < \log M_{\text{sub}} < \log M_h - 0.3$ . The lower limit for  $\log M_{\text{sub}}$  is set since below this, its ESD signal can be ignored. As we have seen in Figure 2 that the BCGs are the best tracers of the halo centers, we focus only this set of ESD measurements.

Figure 5 is an example of marginalized posterior distributions of the five parameters for ESDs in the M1 sample after an MCMC process. Within these five free parameters, we see only the host halo mass  $\log M_h$ , and the off-center distance  $R_{\text{sig}}$  can be well constrained, while the concentration  $c$  is quite strongly correlated with the off-center distance  $R_{\text{sig}}$ . The constraints on the subhalo fraction and subhalo mass are very weak.

We show in Figure 6 the best-fitting results for the groups separated into the four different halo mass bins as well as the ESD contributions for the different mass components. In the mass and radius ranges we consider, the subhalo and two-halo term contributions are quite negligible. This is also the reason

<sup>14</sup> *emcee* is an MIT-licensed pure-Python implementation of Goodman & Weares Affine Invariant Markov Chain Monte Carlo Ensemble sampler.

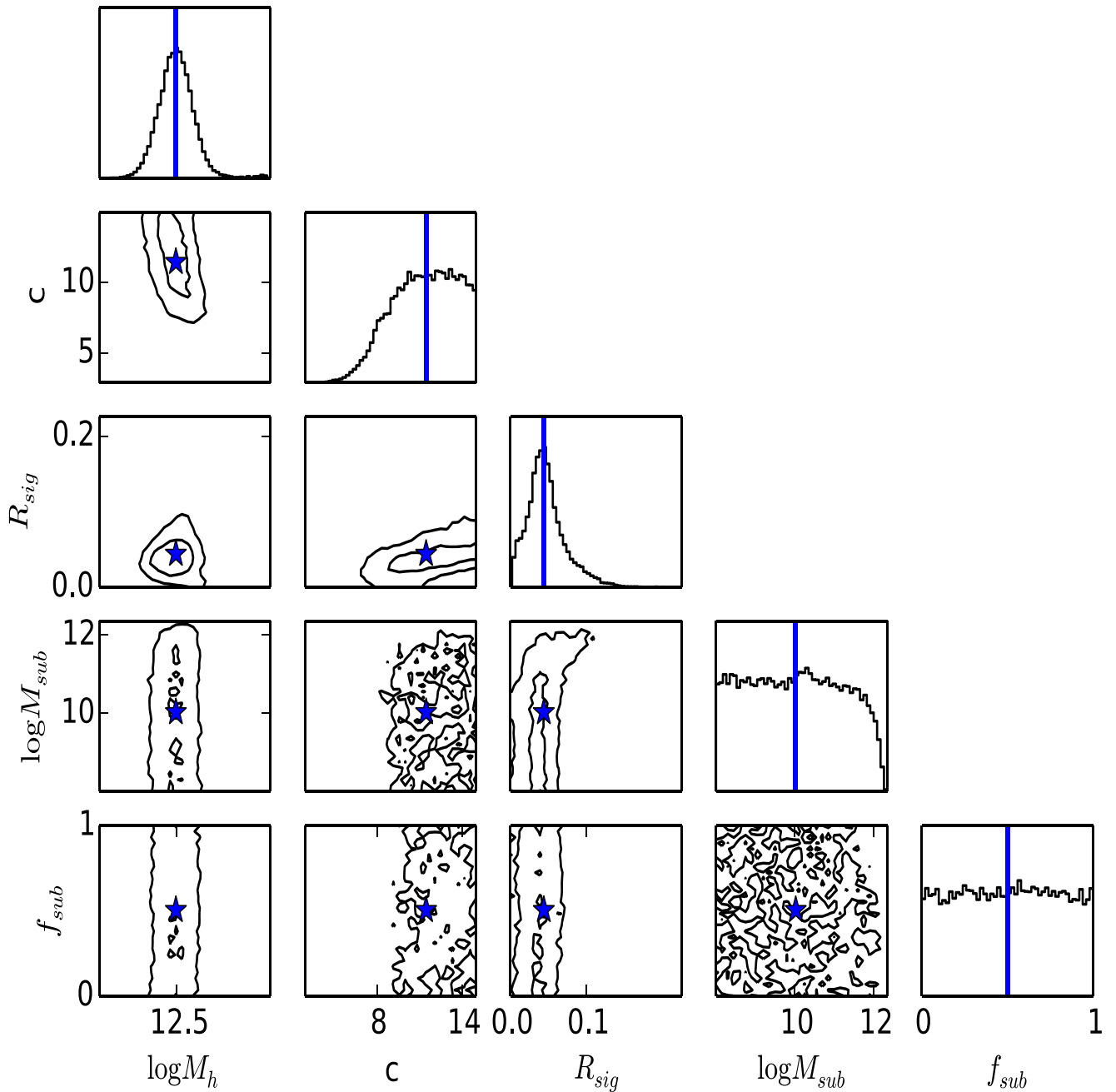


**Figure 5.** The marginalized posterior distributions of the five free parameters for the lowest mass bin groups. The blue stars (blue solid lines) denote the median value of each distribution. The two contour levels correspond to the 68% and 95% confidence levels, respectively.

why we cannot place tight constraints on the subhalo fraction and subhalo mass. The contribution of the stellar mass of the BCG is only important at very small scales. Thus, the observed ESDs in this study can mainly provide us with the constraints on the host halo properties.

Table 3 lists the best-fit parameters for groups in different mass bins. As we have seen from the likelihood distribution of parameters in Figure 5, we can have a fairly good constraint on the halo mass of the group samples. However, if we compare the halo masses obtained from the ESDs with those obtained from the group catalog (c.f. Table 1), they are roughly underestimated by 0.1 to  $\sim 0.2$  dex. We will discuss this discrepancy in the following section. The overall off-center distances for our BCGs are quite small, assuring that BCGs are

indeed good tracers of halo centers. On the other hand, the concentrations of the halos seem to be somewhat larger than the theoretical predictions (e.g., Zhao et al. 2009). However, since the concentration  $c$  and the off-center distance  $R_{\text{sig}}$  are quite tightly correlated, if we adopt the lower value of  $R_{\text{sig}}$ , the concentration  $c$  will drop significantly as well.

Listed in Table 4 are the best-fit parameters for the groups that are separated into the high and low X-ray luminosity subsamples. Although due to the smaller number of lens systems the error for each data point for our X-ray subsamples is somewhat larger and thus the constraints on the five parameters are somewhat weaker, we do see the prominent feature of the halo masses of the high X-ray luminosity subsamples being higher than their low luminosity counterparts

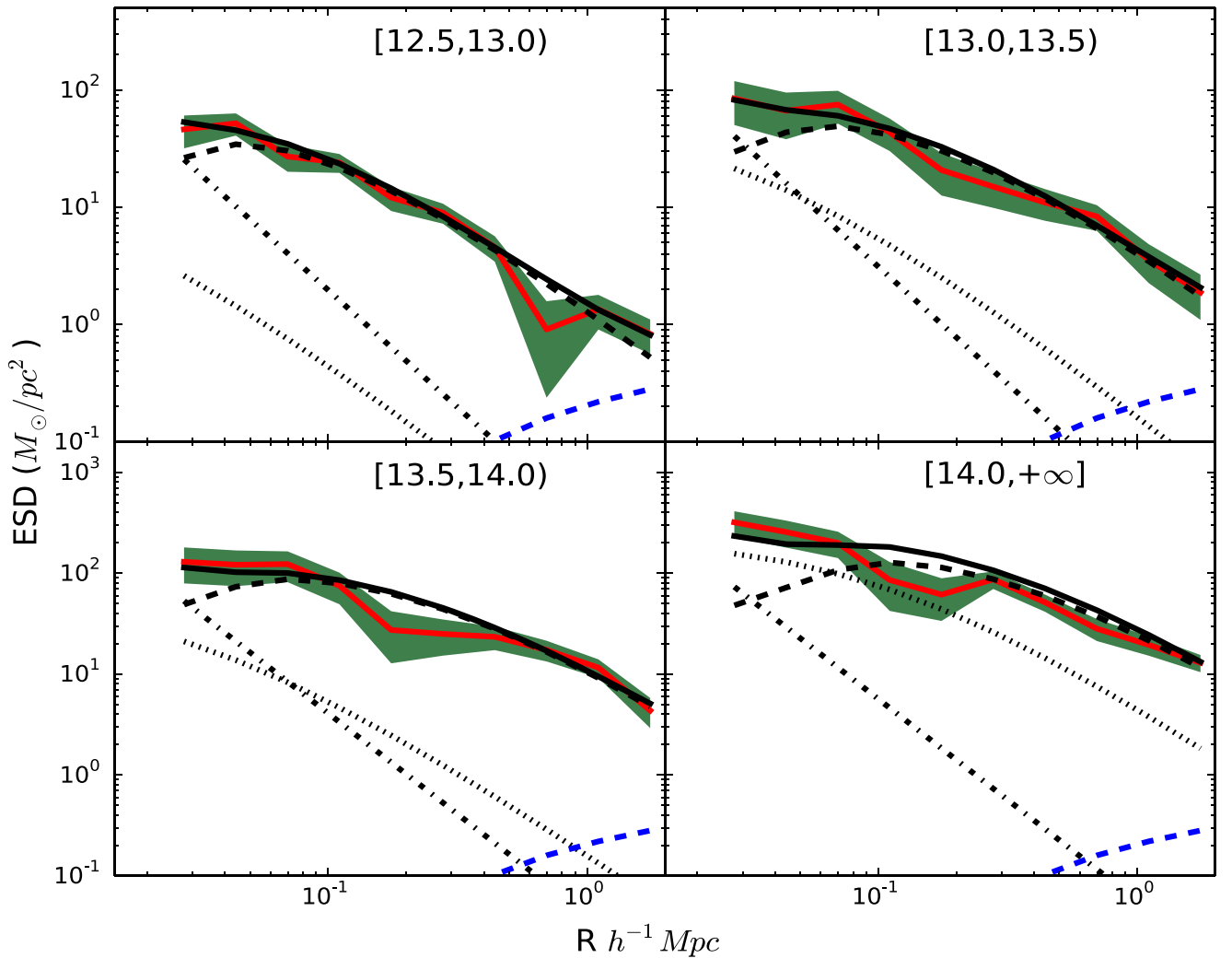


**Figure 6.** The ESD measurements (shaded area) and the best-fit model predictions (black solid line) for groups in the four different mass bins. The dashed, dotted, dotted–dashed, and blue dashed lines are the contributions of an off-centered NFW profile, subhalo, stellar mass of the galaxy under consideration, and the two-halo term, respectively.

**Table 3**  
Posteriors of the Parameters We Fitted to Our Group Samples

Sample	Mass Bin	Centers	$\log M_h$	$c$	$R_{\text{sig}}$	$\log M_{\text{sub}}$	$f_{\text{sub}}$
M1	[12.5–13.0)	BCG	$12.50^{+0.07}_{-0.07}$	$11.35^{+2.41}_{-2.57}$	$0.04^{+0.03}_{-0.02}$	$10.1^{+1.39}_{-1.35}$	$0.49^{+0.34}_{-0.33}$
M2	[13.0–13.5)	BCG	$13.11^{+0.14}_{-0.12}$	$9.19^{+3.45}_{-2.91}$	$0.05^{+0.07}_{-0.03}$	$11.45^{+1.07}_{-2.27}$	$0.57^{+0.30}_{-0.35}$
M3	[13.5–14.0)	BCG	$13.62^{+0.12}_{-0.10}$	$9.19^{+3.45}_{-2.92}$	$0.05^{+0.08}_{-0.03}$	$11.44^{+1.07}_{-2.26}$	$0.56^{+0.29}_{-0.35}$
M4	[14.0–above)	BCG	$14.10^{+0.16}_{-0.10}$	$9.64^{+3.09}_{-2.64}$	$0.08^{+0.13}_{-0.06}$	$13.31^{+0.33}_{-1.73}$	$0.72^{+0.19}_{-0.32}$

in all mass bins. The difference is to 0.2 to  $\sim 0.3$  dex, which means that the high X-ray luminosity subsamples are nearly a factor of 2 more massive than their low X-ray luminosity counterparts.

#### 4. Eddington Bias of the Halo Mass Estimation

Recent studies have shown that the combination of galaxy–galaxy lensing and the clustering of galaxies can be used to constrain cosmology (e.g., Cacciato et al. 2013; More et al. 2013; van den Bosch et al. 2013; Leauthaud et al. 2017), and that the halo masses estimated for groups using galaxy–galaxy lensing signals and hence the halo mass function can also be used to constrain the cosmological parameters. However,

before doing so, one needs to make a careful study of the systematics between the galaxy–galaxy lensing measurement and modeling. Note that the group masses estimated from the ranking of characteristic group luminosity or stellar mass have a typical uncertainty of about 0.3 dex. Thus, the halos/groups binned in terms of group mass may induce an Eddington bias in the galaxy–galaxy lensing halo mass estimation.

Here we make use of a high-resolution  $N$ -body simulation to help us understand the systematics of galaxy–galaxy lensing modeling. Our simulation includes  $3072^3$  dark matter particles in a periodic box  $500 h^{-1}$  Mpc on a side (Li et al. 2016), which was carried out at the Center for High Performance Computing at Shanghai Jiao Tong University. It was run with L-GADGET, a memory-optimized version of GADGET2 (Springel 2005).

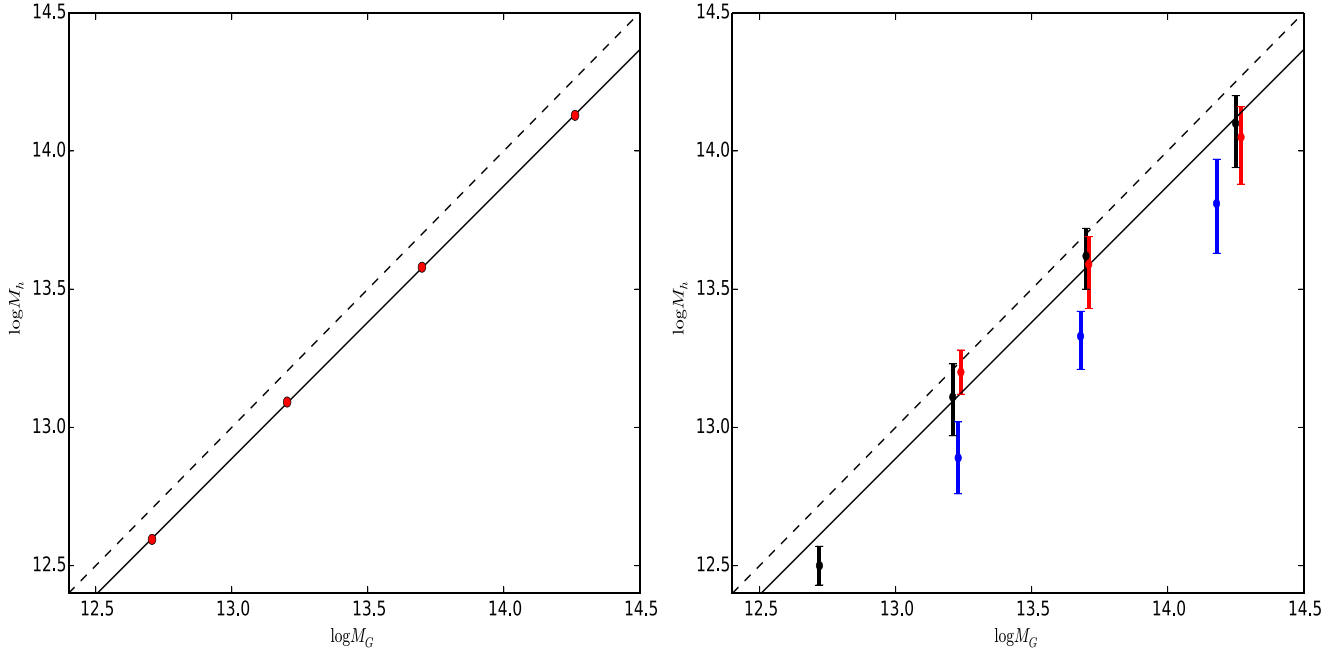


**Figure 7.** Left panel: the average group mass vs. the true halo mass for those groups whose mass estimation has an uncertainty of about 0.3 dex. The solid line, with  $\log M_h = 0.9858 * \log M_G - 0.07168$ , shows the best-fit results, while the dashed line is the one-to-one relation. Right panel: the average group mass estimated using the luminosity ranking in Y07 vs. the halo mass estimated using the galaxy–galaxy lensing signals. The black dots are the results from all of the groups binned in the four group mass bins. The red and blue dots are for the high X-ray luminosity subsamples and low X-ray luminosity subsamples, respectively. The solid line is the same as the one in the left panel.

**Table 4**  
Posteriors of the Parameters We Fitted to Our High and Low X-Ray Luminosity Subsamples

Mass Bin	Centers+X-ray	$\log M_h$	$c$	$R_{\text{sig}}$	$\log M_{\text{sub}}$	$f_{\text{sub}}$
13.0–13.5	BCG+high	$13.20^{+0.08}_{-0.08}$	$11.11^{+2.79}_{-3.61}$	$0.18^{+0.07}_{-0.09}$	$12.06^{+0.52}_{-1.95}$	$0.61^{+0.27}_{-0.31}$
	BCG+low	$12.89^{+0.13}_{-0.13}$	$9.75^{+3.79}_{-3.60}$	$0.11^{+0.17}_{-0.08}$	$11.81^{+0.58}_{-2.25}$	$0.63^{+0.25}_{-0.35}$
	X-ray+high	$13.19^{+0.09}_{-0.08}$	$10.86^{+2.93}_{-3.63}$	$0.17^{+0.07}_{-0.10}$	$11.82^{+0.68}_{-2.25}$	$0.58^{+0.29}_{-0.34}$
	X-ray+low	$12.89^{+0.13}_{-0.13}$	$9.72^{+3.75}_{-3.52}$	$0.11^{+0.19}_{-0.08}$	$11.88^{+0.53}_{-2.15}$	$0.51^{+0.32}_{-0.34}$
13.5–14.0	BCG+high	$13.59^{+0.16}_{-0.10}$	$6.80^{+2.51}_{-1.51}$	$0.06^{+0.08}_{-0.04}$	$11.11^{+1.37}_{-2.09}$	$0.49^{+0.34}_{-0.33}$
	BCG+low	$13.33^{+0.12}_{-0.09}$	$11.28^{+2.37}_{-2.43}$	$0.04^{+0.05}_{-0.03}$	$10.96^{+1.52}_{-2.03}$	$0.52^{+0.32}_{-0.34}$
	X-ray+high	$13.58^{+0.12}_{-0.10}$	$6.87^{+3.01}_{-1.61}$	$0.09^{+0.07}_{-0.05}$	$10.70^{+1.52}_{-1.82}$	$0.48^{+0.34}_{-0.35}$
	X-ray+low	$13.34^{+0.12}_{-0.10}$	$11.29^{+2.39}_{-2.54}$	$0.04^{+0.06}_{-0.03}$	$10.99^{+1.49}_{-2.01}$	$0.53^{+0.32}_{-0.35}$
14.0–above	BCG+high	$14.05^{+0.17}_{-0.11}$	$7.24^{+1.71}_{-1.33}$	$0.04^{+0.05}_{-0.02}$	$11.86^{+1.30}_{-2.58}$	$0.51^{+0.32}_{-0.32}$
	BCG+low	$13.81^{+0.18}_{-0.16}$	$10.36^{+3.07}_{-3.72}$	$0.05^{+0.15}_{-0.03}$	$12.67^{+0.68}_{-2.80}$	$0.69^{+0.23}_{-0.37}$
	X-ray+high	$14.01^{+0.14}_{-0.08}$	$7.17^{+4.85}_{-2.29}$	$0.23^{+0.12}_{-0.18}$	$12.62^{+0.67}_{-2.42}$	$0.56^{+0.29}_{-0.30}$
	X-ray+low	$13.82^{+0.18}_{-0.16}$	$9.88^{+3.37}_{-3.72}$	$0.07^{+0.17}_{-0.05}$	$12.83^{+0.55}_{-2.69}$	$0.70^{+0.29}_{-0.30}$

The cosmological parameters adopted by this simulation are consistent with the *WMAP9* results (Hinshaw et al. 2013; which are very similar to the *WMAP7* results as well), and each particle has a mass of  $3.4 \times 10^8 h^{-1} M_{\odot}$ . Dark matter halos are identified using the standard FOF algorithm with a linking length that is 0.2 times the mean interparticle separation. The mass of halos,  $M_h$ , is simply defined as the sum of the masses of all the particles in the halos, and we remove halos with fewer than 20 particles.

Using the true halos in the simulation, we mimic the halo mass estimation uncertainty in the groups as follows. First, we add to each halo mass a Gaussian scatter with  $\sigma = 0.3$  in log space. Next, we rank all of the resulting halos and match them with the halo mass function model prediction (Tinker et al. 2008) assuming a *WMAP7* cosmology to assign each halo a new mass. Thus, assigned halo masses are referred to as

the group masses  $M_G$ . Following the same mass selection criteria used for our galaxy–galaxy lensing studies, we separate the groups (halos) into four samples. From these four samples, we estimated both the average group mass  $M_G$  and the true halo mass  $M_h$ . The resulting group versus true halo mass relation is shown in the left panel of Figure 7. Obviously, the data points are off from the diagonal dotted line at about the 0.1 dex level, which illustrates a bias between these two halo masses. We use a solid line to fit the data points, which can be used to roughly account for the Eddington bias in our weak galaxy–galaxy lensing studies.

Shown in the right panel of Figure 7 is the average group mass obtained in Y07 versus the halo mass estimated from the galaxy–galaxy lensing signals in our study. For all group samples, after taking into account the Eddington bias, i.e., comparing to the solid line, the data in the three massive group

bins agree very well, indicating that the *WMAP7* cosmology adopted in this study is quite consistent with the lensing mass constraints. On the other hand, according to the result for the lowest mass bin, we still see that the halo mass estimated from the galaxy–galaxy lensing signals is about 0.1 dex lower. Similar trends were also reported in a recent study by Leauthaud et al. (2017), where they found that the lensing signals predicted from clustering are 20%–40% larger than the true measurements. It still remains unclear to us what is the main cause of this lensing deficiency around relatively low-mass halos.

For the groups that are separated into the high and low X-ray luminosity subsamples, we do see that the average halo masses of the low X-ray luminosity subsamples are systematically smaller. Thus, a combination of X-ray luminosity and optical total group luminosity will be useful to better constrain the individual group/cluster mass.

Finally, we caution that when using galaxy–galaxy lensing signals around lens systems to constrain cosmological parameters in future larger surveys, it would be important to take into account the Eddington bias as demonstrated here.

## 5. Summary and Conclusion

We measure the galaxy–galaxy lensing signals around group samples in different mass bins using the source galaxy shape measurements obtained by Luo et al. (2017), where the group masses are provided by Yang et al. (2007) using the ranking of characteristic group luminosities. We also divide the groups with X-ray luminosities obtained by Wang et al. (2014) into high and low X-ray luminosity subsamples and measured their galaxy–galaxy lensing signals separately.

We then modeled the galaxy–galaxy signals by considering contributions from an off-centered NFW profile, subhalo, stellar mass, and two-halo term using five free parameters: halo mass  $\log M_h$ , concentration  $c$ , off-center distance  $R_{\text{sig}}$ , subhalo fraction  $f_{\text{sub}}$ , and subhalo mass  $\log M_{\text{sub}}$ . We then run MCMC to constrain the five free parameters by assigning them with flat priors. From the lensing signals we measured from the SDSS DR7 observation, we are able to provide relatively good constraints on the halo properties, although not on the subhalo properties. Below we summarize the main findings of this work.

1. By checking the galaxy–galaxy lensing signals around four kinds of halo-center tracers—BCGs, LwCens, NwCens, and X-ray peak positions—we find that BCG is the best halo-center tracer.
2. The off-center effect  $R_{\text{sig}}$  for BCGs is roughly at  $0.05 h^{-1}$  Mpc, from  $0.04 h^{-1}$  Mpc for the lowest mass bin group sample to  $0.09 h^{-1}$  Mpc for the most massive group sample.
3. After taking into account the Eddington bias, the halo masses estimated from galaxy–galaxy lensing signals are consistent with the group masses obtained using abundance matching assuming *WMAP7* cosmology in the three massive samples. This consistency implies that the *WMAP7* cosmology is favored by the lensing signals measured in this study.
4. If separated into high and low X-ray luminosity subsamples, the low X-ray luminosity subsamples have overall lower halo masses compared to their high X-ray luminosity counterparts. This X-ray luminosity

segregation in halo mass indicates that we can combine the X-ray luminosities and optical luminosities of groups to better constrain their individual masses.

Finally, as the galaxy–galaxy lensing can provide us with an independent measurement of the halo mass for clusters and groups, for larger and deeper surveys, we can use the resulting halo mass functions to constrain cosmological parameters.

We thank the anonymous referee for helpful comments that greatly improved the presentation of this paper. This work is supported by the 973 Program (Nos. 2015CB857002, 2015CB857001), National Science Foundation of China (Nos. 11233005, 11673016, 11433001, 11503064, 11621303), Chinese Scholarship Council (201504910477), and Shanghai Natural Science Foundation, grant No. 15ZR1446700. L.P.F. acknowledges the support from NSFC grants 11333001 and 11673018, STCSM grants 13JC1404400 and 16R1424800, and SHNU grant DY1201603. We also thank the support of the Key Laboratory for Particle Physics, Astrophysics and Cosmology, Ministry of Education.

## ORCID iDs

Wentao Luo  <https://orcid.org/0000-0003-1297-6142>  
 Xiaohu Yang  <https://orcid.org/0000-0003-3997-4606>  
 Tianhuan Lu  <https://orcid.org/0000-0003-1040-2639>  
 Feng Shi  <https://orcid.org/0000-0002-9968-2894>  
 H. J. Mo  <https://orcid.org/0000-0002-9665-5380>  
 Jiajun Zhang  <https://orcid.org/0000-0002-4117-343X>  
 Nan Li  <https://orcid.org/0000-0001-6800-7389>

## References

- Abazajian, K. N., Adelman-McCarthy, J. K., Agüeros, M. A., et al. 2009, *ApJS*, **182**, 543
- Bacon, D. J., & Taylor, A. N. 2003, *MNRAS*, **344**, 1307
- Bartelmann, M. 1996, *A&A*, **313**, 697
- Bell, E. F., McIntosh, D. H., Katz, N., & Weinberg, M. D. 2003, *ApJS*, **149**, 289
- Bernstein, G. M., & Jarvis, M. 2002, *AJ*, **123**, 583
- Bernstein, G. M., & Armstrong, R. 2014, *MNRAS*, **438**, 1880
- Bertin, E., & Arnouts, S. 1996, *A&AS*, **117**, 393
- Blanton, M. R., Schlegel, D. J., Strauss, M. A., et al. 2005, *AJ*, **129**, 2562
- Bleem, L. E., Stalder, B., de Haan, T., et al. 2015, *ApJS*, **216**, 27
- Cacciato, M., van den Bosch, F. C., More, S., et al. 2009, *MNRAS*, **394**, 929
- Cacciato, M., van den Bosch, F. C., More, S., Mo, H., & Yang, X. 2013, *MNRAS*, **430**, 767
- Eke, V. R., Baugh, C. M., Cole, S., et al. 2004, *MNRAS*, **348**, 866
- Evrard, A. E., MacFarland, T. J., Couchman, H. M. P., et al. 2002, *ApJ*, **573**, 7
- Fischer, P., McKay, T. A., Sheldon, E., et al. 2000, *AJ*, **120**, 1198
- Fu, L., Semboloni, E., Hoekstra, H., et al. 2008, *A&A*, **479**, 9
- George, M. R., Leauthaud, A., Bundy, K., et al. 2012, *ApJ*, **757**, 2
- Heymans, C., Brown, M. L., Barden, M., et al. 2005, *MNRAS*, **361**, 160
- Heymans, C., Van Waerbeke, L., Miller, L., et al. 2012, *MNRAS*, **427**, 146
- Hinshaw, G., Larson, D., Komatsu, E., et al. 2013, *ApJS*, **208**, 19
- Hirata, C., & Seljak, U. 2003, *MNRAS*, **343**, 459
- Johnston, D. E., Sheldon, E. S., Tasitsiomi, A., et al. 2007, *ApJ*, **656**, 27
- Kaiser, N., Squires, G., & Broadhurst, T. 1995, *ApJ*, **449**, 460
- Kitching, T. D., Miller, L., Heymans, C. E., van Waerbeke, L., & Heavens, A. F. 2008, *MNRAS*, **390**, 149
- Kilbinger, M., Fu, L., Heymans, C., et al. 2013, *MNRAS*, **430**, 2200
- Koester, B. P., McKay, T. A., Annis, J., et al. 2007, *ApJ*, **660**, 221
- Kuijken, K., Heymans, C., Hildebrandt, H., et al. 2015, *MNRAS*, **454**, 3500
- Leauthaud, A., Saito, S., Hilbert, S., et al. 2017, *MNRAS*, **467**, 3024
- Lewis, A. 2013, *PhRvD*, **87**, 103529
- Li, R., Shan, H., Kneib, J.-P., et al. 2016, *MNRAS*, **458**, 2573
- LSST Science Collaboration, Abell, P. A., Allison, J., et al. 2009, arXiv:0912.0201
- Lu, Y., Yang, X., & Shen, S. 2015, *ApJ*, **804**, 55

- Luo, W., Yang, X., & Zhang, J. 2017, *ApJ*, **836**, 1
- Lupton, R., Gunn, J. E., Ivezić, Z., Knapp, G. R., & Kent, S. 2001, in ASP Conf. Ser. 238, *Astronomical Data Analysis Software and Systems X*, ed. F. R. Harnden, Jr., F. A. Primini, & H. E. Payne (San Francisco, CA: ASP), 269
- Jarvis, M., Sheldon, E., Zuntz, J., et al. 2016, *MNRAS*, **460**, 2245
- Johnston, D. E., Sheldon, E. S., Wechsler, R. H., et al. 2007, arXiv:0709.1159
- Mandelbaum, R., Hirata, C. M., Seljak, U., et al. 2005, *MNRAS*, **361**, 1287
- Mandelbaum, R., Seljak, U., Kauffmann, G., Hirata, C. M., & Brinkmann, J. 2006, *MNRAS*, **368**, 715
- Maoli, R., Mellier, Y., van Waerbeke, L., et al. 2000, *Msngr*, **101**, 10
- Miller, C. J., Nichol, R. C., Reichart, D., et al. 2005, *AJ*, **130**, 968
- Miller, L., Kitching, T. D., Heymans, C., Heavens, A. F., & van Waerbeke, L. 2007, *MNRAS*, **382**, 315
- Miller, L., Heymans, C., Kitching, T. D., et al. 2013, *MNRAS*, **429**, 2858
- More, S., van den Bosch, F. C., Cacciato, M., et al. 2013, *MNRAS*, **430**, 747
- Navarro, J. F., Frenk, C. S., & White, S. D. M. 1997, *ApJ*, **490**, 493
- Niemiec, A., Jullo, E., Limousin, M., et al. 2017, *MNRAS*, **471**, 1153
- Pratt, G. W., Croston, J. H., Arnaud, M., & Böhringer, H. 2009, *A&A*, **498**, 361
- Refregier, A. 2003, *ARA&A*, **41**, 645
- Refregier, A., Amara, A., Kitching, T. D., et al. 2010, arXiv:1001.0061
- Rhodes, J., Refregier, A., & Groth, E. J. 2000, *ApJ*, **536**, 79
- Rykoff, E. S., Rozo, E., Busha, M. T., et al. 2014, *ApJ*, **785**, 104
- Seljak, U., & Warren, M. S. 2004, *MNRAS*, **355**, 129
- Sheldon, E. S., Johnston, D. E., Frieman, J. A., et al. 2004, *AJ*, **127**, 2544
- Shi, F., Yang, X., Wang, H., et al. 2017, arXiv:1712.04163
- Simet, M., McClintock, T., Mandelbaum, R., et al. 2017, *MNRAS*, **466**, 3103
- Springel, V. 2005, *MNRAS*, **364**, 1105
- Sunyaev, R. A., & Zeldovich, Y. B. 1972, *CoASP*, **4**, 173
- Takahashi, R., Sato, M., Nishimichi, T., Taruya, A., & Oguri, M. 2012, *ApJ*, **761**, 152
- Tinker, J. L., Weinberg, D. H., Zheng, Z., & Zehavi, I. 2005, *ApJ*, **631**, 41
- Tinker, J., Kravtsov, A. V., Klypin, A., et al. 2008, *ApJ*, **688**, 709
- van den Bosch, F. C., Norberg, P., Mo, H. J., & Yang, X. 2004, *MNRAS*, **352**, 1302
- van den Bosch, F. C., More, S., Cacciato, M., Mo, H., & Yang, X. 2013, *MNRAS*, **430**, 725
- Viola, M., Cacciato, M., Brouwer, M., et al. 2015, *MNRAS*, **452**, 3529
- Wang, L., Yang, X., Shen, S., et al. 2014, *MNRAS*, **439**, 611
- Wechsler, R. H., Zentner, A. R., Bullock, J. S., Kravtsov, A. V., & Allgood, B. 2006, *ApJ*, **652**, 71
- Yang, X., Mo, H. J., van den Bosch, F. C., & Jing, Y. P. 2005, *MNRAS*, **356**, 1293
- Yang, X., Mo, H. J., van den Bosch, F. C., et al. 2006, *MNRAS*, **373**, 1159
- Yang, X., Mo, H. J., van den Bosch, F. C., et al. 2007, *ApJ*, **671**, 153
- York, D. G., Adelman, J., Anderson, J. E., Jr., et al. 2000, *AJ*, **120**, 1579
- Zhang, J. 2010, *MNRAS*, **403**, 673
- Zhang, J. 2011, *JCAP*, **11**, 041
- Zhang, J., Luo, W., & Foucaud, S. 2015, *JCAP*, **1**, 024
- Zhang, J. 2016, *Natl. Sci. Rev.*, **3**, 159
- Zhao, D. H., Jing, Y. P., Mo, H. J., & Börner, G. 2009, *ApJ*, **707**, 354
- Zu, Y., Weinberg, D. H., Jennings, E., Li, B., & Wyman, M. 2014, *MNRAS*, **445**, 1885
- Zu, Y., & Weinberg, D. H. 2013, *MNRAS*, **431**, 3319